

Confined growth of armchair MoS₂ nanotubes at the 1-nm limit

Yusuke Nakanishi,^{1,2,3*} Ryosuke Senga,^{4*} Shinpei Furusawa,³ Yuta Sato,⁴ Zheng Liu,^{5,6} Takumi Tanaka,³ Yanlin Gao,^{7,8} Mina Maruyama,^{7,8} Susumu Okada,^{7,8} Yasumitsu Miyata,⁹ and Kazu Suenaga^{6*}

Affiliations:

¹Department of Advanced Materials Science, The University of Tokyo; Kashiwa, 277-8651, Japan.

²Research Center for Magnetic and Spintronic Materials, National Institute for Materials Science (NIMS); Tsukuba 305-0047, Japan.

³Department of Physics, Tokyo Metropolitan University; Hachioji, 192-0397, Japan.

⁴Research Institute of Core Technology for Materials Innovation, National Institute of Advanced Industrial Science and Technology (AIST); Tsukuba, 305-8565, Japan.

⁵Multi-Material Research Institute, National Institute of Advanced Industrial Science and Technology (AIST); Nagoya, 463-8560, Japan.

⁶SANKEN (The Institute of Scientific and Industrial Research), The University of Osaka; Osaka, 567-0047, Japan.

⁷Department of Physics, University of Tsukuba; Tsukuba, 305-8571, Japan.

⁸Tsukuba Institute for Advanced Research (TIAR), University of Tsukuba; Tsukuba, 305-8577, Japan.

⁹Research Center for Materials Nanoarchitectonics, National Institute for Materials Science (NIMS); Tsukuba, 305-0044, Japan.

*Corresponding author. Email: naka24ysk@edu.k.u-tokyo.ac.jp
ryosuke-senga@aist.go.jp
suenaga-kazu@sanken.osaka-u.ac.jp

Abstract: Atomically thin nanotubes of semiconducting transition metal dichalcogenides offer a platform for exploring quantum phenomena at the one-dimensional limit and for realizing nanoscale transistor channels. Yet, conventional syntheses produce only large-diameter (>10 nm), multiwalled tubes with uncontrolled chiralities. We report the synthesis of single-walled molybdenum disulfide (MoS₂) nanotubes with diameters approaching 1 nm, achieved through spatially confined reactions inside boron nitride (BN) nanotubes. The confined geometry stabilizes otherwise inaccessible, highly strained MoS₂ nanotubes, yielding structurally well-defined armchair configurations. Their bandgaps shrink systematically with decreasing diameter, in accord with long-standing theoretical predictions. The insulating BN sheath simultaneously provides an intrinsic gate-all-around architecture, thereby promising access to truly nanoscale transistor channels.

Main Text:

The inability to control the atomic structure of one-dimensional (1D) semiconductors remains a major barrier to realizing truly nanoscale transistor channels. Semiconducting transition metal dichalcogenide nanotubes (TMD NTs) are especially attractive because their cylindrical geometry inherently lends itself to all-around electrostatic gating (1–3), while avoiding the chirality-induced metallicity that limits carbon NTs (4). Beyond their technological merits, TMD NTs exhibit exotic quantum phenomena such as non-reciprocal superconductivity (5) and bulk photovoltaic effects (6). At few-nanometer diameters, theory further predicts emergent behaviors absent in layered TMDs, including chirality-dependent electronic structures (7), diameter-tunable bandgaps (8), and giant built-in polarizations (9). Few-nanometer TMD NTs thus display 1D physical properties governed by their atomic structure and symmetry breaking, and provide new degrees of freedom for engineering nanoscale semiconductor channels.

Yet, the experimental realization of ultrafine TMD NTs has remained elusive. Conventional vapor–gas–solid reactions yield large-diameter (>10 nm), multiwalled structures with mixed chiralities (10, 11). A recently developed template-assisted approach—wrapping TMD layers coaxially around other NTs—produces single-walled (SW) species that remain 5–10 nm in diameter and exhibit uncontrolled structures (12–14). These limitations ultimately stem from the steep elastic energy for bending a three-atom-thick TMD layer, which rises sharply at small diameters (15), rendering few-nanometer species intrinsically unstable.

We report the synthesis of SW-MoS₂ NTs with diameters approaching 1 nm via spatially confined reactions inside boron nitride (BN) NTs (Fig. 1A). The insulating BN sheath stabilizes otherwise inaccessible, highly strained MoS₂ NTs and provides an intrinsic gate-all-around geometry (Fig. 1B). Significantly, the resulting few-nanometer MoS₂ NTs display a strong armchair preference ($\theta \approx 30^\circ$). Monochromated electron energy-loss spectroscopy (EELS) reveals a systematic reduction in bandgap with decreasing diameter, consistent with theoretical expectations (Fig. 1C) yet opposite to the trend observed in carbon NTs. These findings establish confined growth as a powerful route to atomically precise 1D semiconductors, pointing toward truly nanoscale transistor channels.

Confined growth of MoS₂ NTs within BN NT

s

Few-nanometer SW-MoS₂ NTs were synthesized by annealing Mo₄S₄ clusters confined in BN NTs (Fig. 2A). Mo₄S₄ precursors were first inserted into BN NTs through a vapor-phase reaction (16), in which MoCl₅ and sulfur was heated together with end-opened BN NTs under high vacuum ($\sim 10^{-7}$ hPa). This process loads cubic Mo₄S₄ clusters into the BN NT cavities. Subsequent annealing converts the encapsulated clusters into NTs. NT formation occurs below 700 °C, while elevated temperatures favor ribbon-like products (17). Thus, reaction temperature provides a simple way to synthesize different 1D Mo–S architectures. The transformation proceeds through cluster coalescence followed by atomic reconstruction (fig. S1), although the pathway to the selective NT formation at low temperatures remains to be clarified.

The atomic structure of the products was examined by Z-contrast high-angle annular dark-field scanning transmission electron microscopy (HAADF-STEM). A representative HAADF image (Fig. 2B) shows coaxial 1D structures inside BN NTs. Since the intensity of HAADF images reflects the atomic number (Z-contrast) (18), the brighter inner feature indicates that the encapsulated products comprise heavier elements than B and N. Atomic-resolution imaging shows a crystalline NT nested within the BN NT (Fig. 2C). Closer inspection reveals moiré patterns arising from superposition of the front and back walls. EELS elemental maps further identify Mo and S from the inner products (Fig. 2D). An EEL spectrum collected from the same region displays

a shift in the S L_2 edge, consistent with chemical conversion during annealing (fig. S2). Fast Fourier transform (FFT) analysis resolves a six-fold symmetry corresponding to the $\{100\}$ planes of hexagonal MoS_2 with a spacing of 0.27 ± 0.2 nm (Fig. 2E), in accord with the atomic arrangement seen in the magnified HAADF image (Fig. 2F). Raman spectra collected from filled BN NTs exhibit characteristic MoS_2 modes consistent with curvature-induced strain (fig. S3). These results confirm the confined growth of SW- MoS_2 NTs within BN NTs.

Geometrical analyses of SW- MoS_2 NTs

Further STEM imaging resolves the structural characteristics of the encapsulated MoS_2 NTs. Under the present conditions, SW species dominate, typically reaching lengths of 50–100 nm, occasionally extending to 150–200 nm ($\sim 5\%$) (fig. S4). In contrast, multiwalled structures are strongly suppressed: double-walled (DW) species were rarely observed ($<1\%$) (fig. S5), and no thicker species appeared. This absence of multiwall formation reflects the narrow inner cavities of the BN NTs (1–3 nm). The NT-templated chemical vapor deposition approach yielded only trace amounts of encapsulated MoS_2 NTs with short lengths (~ 20 nm) (14), highlighting the advantage of this confinement strategy.

A remarkable feature of the encapsulated MoS_2 NTs is their exceptionally small diameter. Fig. 3A displays representative HAADF images of the resulting SW- MoS_2 NTs with diameters of 1.8 nm, 1.5 nm, and 1.2 nm. Statistical analysis reveals a strong preference for sub-2-nm diameters (Fig. 3B). The mean diameter is 1.9 ± 0.1 nm, which is comparable to carbon NTs yet challenging to achieve. The narrowest NTs observed in the present study have diameters approaching 1 nm (Inset of Fig. 3B). Although certain BN NT cavities are capable of accommodating smaller diameters (14), MoS_2 NTs below ~ 1 nm were not observed, indicating a practical lower limit.

The diameters of the MoS_2 NTs are well constrained by the inner diameters of the BN NTs. The MoS_2 NTs conform to the innermost BN NT walls with a diameter difference of ~ 1 nm (Fig. 3C, fig. S6). This interwall spacing (~ 0.5 nm) corresponds to the interlayer distance in vertical $h\text{BN}/\text{MoS}_2$ heterostructures (19), indicating weak van der Waals (vdW) coupling rather than covalent bonding between MoS_2 and BN walls. Thus, the intrinsic electronic structure of the resulting MoS_2 NTs is largely preserved within the insulating BN NT cavities. Theory predicts that the strain energy of MoS_2 NTs increases inversely with the square of the diameter (8), resulting in steep curvature-induced strain at small diameters. In the confined geometry, however, interwall vdW interactions stabilize these highly curved NTs down to ~ 1 nm.

Aberration-corrected TEM imaging further reveals a pronounced chiral selectivity. The chiral angle θ is defined as the angle between the zigzag direction and the circumferential vector ($0^\circ \leq \theta \leq 30^\circ$) (fig. S7). Chiral angles were determined from FFT analyses using well-established procedures (20, 21). A representative high-resolution TEM image of the encapsulated SW- MoS_2 NTs is presented in Fig. 3D. The corresponding FFT pattern displays hexagonal reflections from both the host BN and the guest MoS_2 (Fig. 3E). For chiral configurations ($0^\circ < \theta < 30^\circ$), the two opposing sidewalls yield mirrored hexagonal patterns, whereas achiral configurations ($\theta = 0^\circ$ and 30°) show a single set of reflections. The FFT pattern of the DW-BN NT exhibits two chiral angles (pink and cyan), whereas the MoS_2 NT shows a single hexagonal pattern (yellow) aligned with the tube axis, corresponding to the armchair configuration ($\theta = 30^\circ$).

Extensive analysis of 172 individual SW- MoS_2 NTs reveals a striking chiral-angle distribution. While the host BN NTs cover the full range of chiral angles from zigzag to armchair (fig. S8), the encapsulated MoS_2 NTs show a strong armchair preference. Statistical analysis confirms that armchair and near-armchair ($24^\circ \leq \theta \leq 30^\circ$) configurations are highly enriched (Fig. 3F), with pure armchair species most abundant (table S1). Right- and left-handed variants were not distinguished in the present study.

No clear correlation is observed in the present analysis between the chiral angles of the guest MoS₂ NTs and those of the host BN NTs. Typically, BN NTs comprise multiple concentric walls with complex stacking, making it challenging to determine the chirality of individual BN walls. We therefore focused on rarely observed SW- and DW-BN NTs, in which the chiral angles of individual walls can be resolved (fig. S9). In these structures, the inner BN walls exhibit chiral angles spanning a wide range without discernible bias (table S2). Moreover, the chiral angles of the encapsulated MoS₂ NTs show no systematic relationship with that of the inner BN NTs (figs. S10 and S11). These findings do not support epitaxial alignment with the BN lattice as the origin of the armchair selectivity of the MoS₂ NTs. A similar absence of chirality correlation has been reported in coaxial carbon/BN NTs (22). Unlike atomically flat 2D interfaces, the intrinsic curvature of NTs does not readily allow epitaxial registry.

Chirality distribution of the encapsulated SW-MoS₂ NTs

A polar plot of the chiral angle as a function of diameter highlights a pronounced size-dependent selectivity (Fig. 4). At relatively larger diameters (3–5 nm), the MoS₂ NTs show a broad spread of chiral angles (blue diamond). In contrast, armchair configurations dominate once the diameter falls below ~2 nm (~84%). Index assignment reveals that narrow MoS₂ NTs overwhelmingly adopt (*n*, *n*) armchair structures for *n* = 6–9, with a minor fraction of near-armchair variants (fig. S12). This sharp selectivity is absent in MoS₂ NTs grown on the outer surfaces of BN NTs (gray circle). Chemical vapor deposition proceeds through freely diffusing vapor-phase intermediates on the BN NT surfaces; as a result, crystal growth proceeds isotropically, yielding a random chirality distribution. The stark contrast between interior and exterior growth highlights a fundamental difference in their underlying growth mechanisms. Notably, the narrowest observed armchair species (~1 nm) corresponds to a (5, 5) configuration. Strain-energy calculations show that armchair configurations below 1 nm cannot sustain a stable cylindrical geometry (fig. S13), indicating that this confined system realizes the practical armchair limit of MoS₂ NTs.

To understand the origin of this selectivity, we compared the strain energies of armchair (7, 7) and zigzag (12, 0) MoS₂ NTs (~1.2 nm diameter) using first-principles structural optimizations. Both structures possess nearly identical total energies (0.30 and 0.31 eV per atom), with inner sulfur displacements that relieve steric repulsion (fig. S14). These results indicate that the observed armchair preference cannot be explained by differences in equilibrium stability. Instead, the selectivity is likely governed by a kinetically controlled mechanism under 1D confinement. Within narrow BN NT cavities (<3 nm), motion of the precursor clusters is spatially restricted such that growth proceeds predominantly along the axial direction. This geometric constraint may favor the formation of armchair and near-armchair configurations in the sub-2-nm regime. This interpretation is consistent with the highly ordered alignment of the precursors inside BN NTs (16), suggesting that spatial confinement may imprint the initial molecular configuration onto the final chirality. A full elucidation of the kinetic pathways will require further *in situ* observations and theoretical modeling.

Optical response of SW-MoS₂ NTs with few-nanometer diameters

Finally, we probed the optical response of individual SW-MoS₂ NTs using monochromated low-loss EELS (Fig. 5A). A representative spectrum from a 1.6-nm-diameter SW-MoS₂ NT (Fig. 5B) shows broad absorption features between 1–5 eV. BN NTs are optically inert in the visible range and exhibit phonon and polariton modes in the infrared region, together with exciton and interband (π – π^*) transitions at 6–8 eV. Therefore, the observed visible-range features arise only from the encapsulated MoS₂ NT (23). In contrast to discrete A, B, and C excitons of monolayer

MoS₂ (24), ultrafine MoS₂ NTs exhibit a broadband continuum, indicating that excitonic dynamics are strongly altered by 1D confinement.

To rationalize this behavior, we computed the electronic density of states (DOS) of MoS₂ NTs using density functional theory (DFT). Both zigzag (12, 0) and armchair (7, 7) species exhibit pronounced van Hove singularities characteristic of 1D systems (fig. S15). Notably, the armchair (7, 7) configuration shows a broadened DOS onset at the conduction-band edge. Based on prior theoretical analyses (25), this broadening can be attributed to the lifting of band degeneracy, resulting in non-degenerate energy levels. Independently, for armchair species, the valence-band maximum near the Γ point flattens at small diameters, giving rise to non-localized electronic transitions. In addition, few-nanometer armchair and near-armchair variants have been predicted to be indirect-gap semiconductors (7), suppressing direct optical transitions. These theoretical features account for the emergence of a broadband continuum in ultrafine MoS₂ NTs.

The absorption onset shows a clear dependence on diameter. Armchair and near-armchair species with diameters of 1–3 nm were examined by monochromated EELS (Fig. 5C–F, table S3). All the NTs display red-shifted onsets (1.3–1.5 eV) relative to monolayer MoS₂ (~1.8 eV). The onset energy decreases monotonically with decreasing diameter, providing direct experimental evidence of diameter-dependent bandgap narrowing in MoS₂ NTs below 3.5 nm. This trend is consistent with long-standing theoretical predictions (8). A comparison with DFT-calculated gaps (fig. S16) shows the same monotonic decrease with decreasing diameter. The remaining differences are attributed to excitonic effects, as EELS probes electron–hole excitations whereas DFT yields ground-state Kohn–Sham gaps. Unlike carbon NTs, curvature-induced bandgap narrowing in MoS₂ NTs arises from perturbation of hybridized Mo *d*–S *p* states, raising the valence-band maximum and lowering the conduction-band minimum (26). The confined 1D environment imposes exceptionally large curvature, stabilizing highly strained compound semiconductor NTs inaccessible by conventional synthesis. This extreme curvature fundamentally modulates the electronic structure of layered MoS₂, providing a direct means to engineer the electronic and optical properties of layered vdW materials.

Outlook

This confinement strategy offers a general route to ultrafine NTs across diverse TMDs (27) and other layered materials, extending nanotube science beyond carbon-based systems. Such structural control enables rational tuning of electronic structure, light–matter interactions, and charge and thermal transport at the 1D limit. For semiconducting NTs, these 1D vdW heterostructures represent an atomically sharp analogue of gate-all-around transistor channels, pointing toward ultimately scaled nanoscale electronics.

References and Notes

1. R. Tenne, L. Margulis, M. Genut, G. Hodes, Polyhedral and cylindrical structures of tungsten disulphide. *Nature* **360**, 444–446 (1992).
2. Y. Feldman, E. Wasserman, D. J. Srolovitz, R. Tenne, High-rate, gas-phase growth of MoS₂ nested inorganic fullerenes and nanotubes. *Science* **267**, 222–225 (1995).
3. J. L. Musfeldt, Y. Iwasa, R. Tenne, Nanotubes from layered transition metal dichalcogenides. *Phys. Today* **73**, 42–48 (2020).
4. R. Saito, G. Dresselhaus, M. Dresselhaus, *Physical properties of carbon nanotubes* (Imperial College Press, London, 1998).

5. F. Qin, W. Shi, T. Ideue, M. Yoshida, A. Zak, R. Tenne, T. Kikitsu, D. Inoue, D. Hashizume, Y. Iwasa, Superconductivity in a chiral nanotube. *Nat. Commun.* **8**, 14465 (2017).
6. Y. Zhang, T. Ideue, M. Onga, F. Qin, R. Suzuki, A. Zak, R. Tenne, J. Smet, Y. Iwasa, Enhanced intrinsic photovoltaic effect in tungsten disulfide nanotubes. *Nature* **7761**, 349–353 (2019).
7. D.-B. Zhang, T. Dumitrică, G. Seifert, Helical nanotube structures of MoS₂ with intrinsic twisting: An objective molecular dynamics study. *Phys. Rev. Lett.* **104**, 065502 (2010).
8. G. Seifert, H. Terrones, M. Terrones, G. Jungnickel, T. Frauenheim, Structure and electronic properties of MoS₂ nanotubes. *Phys. Rev. Lett.* **85**, 146–149 (1999).
9. B. Kim, N. Park, J. Kim, Giant bulk photovoltaic effect driven by the wall-to-wall charge shift in WS₂ nanotubes. *Nat. Commun.* **13**, 3237 (2022).
10. P. Chithaiah, S. Ghosh, A. Idelevich, L. Rovinsky, T. Livneh, A. Zak, Solving the “MoS₂ nanotubes” synthetic enigma and elucidating the route for their catalyst-free and scalable production. *ACS Nano* **14**, 3004–3016 (2020).
11. V. Kunderát, R. Rosentsveig, K. Bukvišová, D. Citterberg, M. Kolíbal, S. Keren, I. Pinkas, O. Yaffe, A. Zak, R. Tenne, Submillimeter-long WS₂ nanotubes: The pathway to inorganic buckypaper. *Nano Lett.* **23**, 10259–10266 (2023).
12. R. Xiang, T. Inoue, Y. Zheng, A. Kumamoto, Y. Qian, Y. Sato, M. Liu, D. Tang, D. Gokhale, J. Guo, K. Hisama, S. Yotsumoto, T. Ogamoto, H. Arai, Y. Kobayashi, H. Zhang, B. Hou, A. Anisimov, M. Maruyama, Y. Miyata, S. Okada, S. Chiashi, Y. Li, J. Kong, E. I. Kauppinen, Y. Ikuhara, K. Suenaga, S. Maruyama, One-dimensional van der Waals heterostructures. *Science* **367**, 537–542 (2020).
13. S. Furusawa, Y. Nakanishi, Y. Yomogida, Y. Sato, Y. Zheng, T. Tanaka, K. Yanagi, K. Suenaga, S. Maruyama, R. Xiang, Y. Miyata, Surfactant-assisted isolation of small-diameter boron-nitride nanotubes for molding one-dimensional van der Waals heterostructures. *ACS Nano* **16**, 16636–16644 (2022).
14. Y. Nakanishi, S. Furusawa, Y. Sato, T. Tanaka, Y. Yomogida, K. Yanagi, W. Zhang, H. Nakajo, S. Aoki, T. Kato, K. Suenaga, Y. Miyata, Structural diversity of single-walled transition metal dichalcogenide nanotubes grown via template reaction. *Adv. Mater.* **35**, 2306631 (2023).
15. G. Seifert, T. Köhler, R. Tenne, Stability of metal chalcogenide nanotubes. *J. Phys. Chem. B* **106**, 2497–2501 (2002).
16. Y. Nakanishi, N. Kanda, M. Aizaki, K. Hirata, Y. Takahashi, T. Endo, Y. Lin, R. Senga, K. Suenaga, S. Aoyagi, M. Maruyama, Y. Gao, S. Okada, Y. Miyata, Z. Liu, Superatomic layer of cubic Mo₄S₄ clusters connected by Cl cross-linking. *Adv. Mater.* **36**, 2404249 (2024).
17. T. Tanaka, Y. Sato, M. Aizaki, S. Furusawa, R. Senga, K. Suenaga, T. Endo, Y. Miyata, Y. Nakanishi, Confined growth of few-nanometer MoS₂ nanoribbons with optical anisotropy in insulating nanotubes. *Nano Lett.* **25**, 14645–14652 (2025).
18. O. L. Krivanek, M. F. Chisholm, V. Nicolosi, T. J. Pennycook, G. J. Corbin, N. Dellby, M. F. Murfitt, C. S. Own, Z. S. Szilagy, M. P. Oxley, S. T. Pantelides, S. J. Pennycook, Atom-by-atom structural and chemical analysis by annular dark-field electron microscopy. *Nature* **464**, 571–574 (2010).

19. Aidan. P. Rooney, A. Kozikov, A. N. Rudenko, E. Prestat, M. J. Hamer, F. Withers, Y. Cao, K. S. Novoselov, M. I. Katsnelson, R. Gorbachev, S. J. Haigh, Observing imperfection in atomic interfaces for van der Waals heterostructures. *Nano Lett.* **17**, 5222–5228 (2017).
20. M. Sadan, L. Houben, A. N. Enyashin, G. Seifert, R. Tenne, Atom by atom: HRTEM insights into inorganic nanotubes and fullerene-like structures. *Proc. Natl. Acad. Sci. U.S.A.* **105**, 15643–15648 (2008).
21. Y. Chen, H. Deniz, L.-C. Qin, Accurate measurement of the chirality of WS₂ nanotubes. *Nanoscale* **9**, 7124–7134 (2017).
22. Y. Zheng, A. Kumamoto, K. Hisama, K. Otsuka, G. Wickerson, Y. Sato, M. Liu, T. Inoue, S. Chiashi, D.-M. Tang, Q. Zhang, A. Anisimov, E. I. Kauppinen, Y. Li, K. Suenaga, Y. Ikuhara, S. Maruyama, R. Xiang, One-dimensional van der Waals heterostructures: Growth mechanism and handedness correlation revealed by nondestructive TEM. *Proc. Natl. Acad. Sci. U.S.A.* **118**, e2107295118 (2021).
23. R. Arenal, O. Stéphan, M. Kociak, D. Taverna, A. Loiseau, C. Colliex, Electron energy loss spectroscopy measurement of the optical gaps on individual boron nitride single-walled and multiwalled nanotubes. *Phys. Rev. Lett.* **95**, 127601 (2005).
24. D. Y. Qiu, F. H. da Jornada, S. G. Louie, Optical spectrum of MoS₂: Many-body effects and diversity of exciton states. *Phys. Rev. Lett.* **111**, 216805 (2013).
25. M. Liu, H. Kaoru, Y. Zheng, M. Maruyama, S. Seo, A. Anisimov, T. Inoue, E. I. Kauppinen, S. Okada, S. Chiashi, R. Xiang, S. Maruyama, Photoluminescence from single-walled MoS₂ nanotubes coaxially grown on boron nitride nanotubes. *ACS Nano* **5**, 8418–8426 (2021).
26. K. Hisama, M. Maruyama, S. Chiashi, S. Maruyama, S. Okada, Indirect-to-direct band gap crossover of single walled MoS₂ nanotubes. *Jpn. J. Appl. Phys.* **60**, 065002 (2021).
27. M. Chhowalla, H. Shin, G. Eda, L.-J. Li, K. Loh, H. Zhang, The chemistry of two-dimensional layered transition metal dichalcogenide nanosheets. *Nat. Chem.* **5**, 263–275 (2013).
28. F. Yao, W. Li, Y. Zhang, C. Jin, Atomic-scale visualization of spontaneous bilayer MoS₂ nanoribbon scrolling via coupled rotation-bending within carbon nanotubes. *ACS Nano* **19**, 34418–34428 (2025).
29. W. H. Chae, J. D. Cain, E. D. Hanson, A. A. Murthy, V. P. Dravid, Substrate-induced strain and charge doping in CVD-grown monolayer MoS₂. *Appl. Phys. Lett.* **111**, 143106 (2017).
30. Z. Liu, K. Suenaga, H. Yoshida, T. Sugai, H. Shinohara, S. Iijima, Determination of optical isomers for left-handed or right-handed chiral double-wall carbon nanotubes. *Phys. Rev. Lett.* **95**, 187406 (2005).

Acknowledgments: The authors acknowledge I. Kondo, P. K. Gogoi, and J. Hong for their assistance in TEM/STEM observation. This work was partially supported by ERATO “Magnetic Thermal Management Materials” from JST, Japan.

Funding:

Japan Science and Technology Agency PRESTO grant JPMJPR23H5

Japan Science and Technology Agency CREST grant JPMJCR20B1

Japan Science and Technology Agency FOREST grant JPMJFR213X

Japan Society for the Promotion of Science KAKENHI grant JP21H05232
Japan Society for the Promotion of Science KAKENHI grant JP21H05234
Japan Society for the Promotion of Science KAKENHI grant JP21H05235
Japan Society for the Promotion of Science KAKENHI grant JP22H00283
Japan Society for the Promotion of Science KAKENHI grant JP22H04957
Japan Society for the Promotion of Science KAKENHI grant JP23H01807
Japan Society for the Promotion of Science KAKENHI grant JP23H00277
Japan Society for the Promotion of Science KAKENHI grant JP24H00044
Japan Society for the Promotion of Science KAKENHI grant JP25K08442
Japan Society for the Promotion of Science KAKENHI grant JP25K22198
Noguchi Shitagau Research grant NJ202408
JKA2025 promotion funds grant 2025M-498

Author contributions:

Conceptualization: YN, KS
Methodology: YN, RS, SO, YM, KS
Investigation: YN, SF, RS, ZL, YS, TT, YG, MM
Visualization: YN
Funding acquisition: YN, KS
Project administration: KS
Supervision: YM, KS
Writing – original draft: YN
Writing – review & editing: YN, RS, KS

Competing interests: Authors declare that a patent application covering the technology described in the manuscript has been filed by JST, and that YN and SF are listed as inventors..

Data and materials availability: All data are available in the main text or the supplementary materials.

Supplementary Materials

Materials and Methods

Supplementary Text

Figs. S1 to S16

Tables S1 to S3

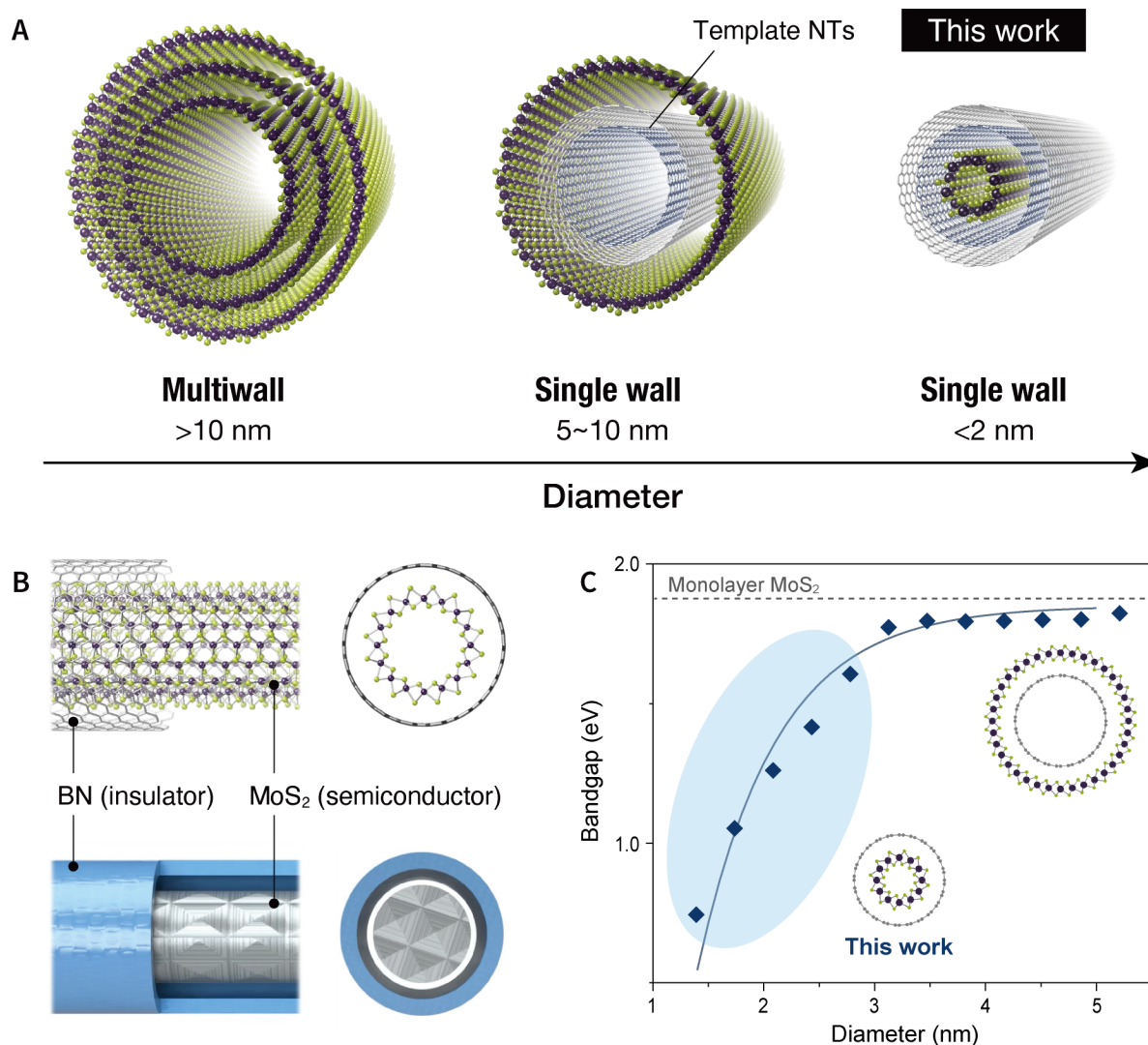


Fig. 1. Structural and electronic characteristics of confined MoS₂ NTs. (A) Schematic comparison of representative MoS₂ NTs. Left: multiwalled MoS₂ NTs (>10 nm diameter) typically obtained by conventional bulk syntheses. Middle: SW-MoS₂ NTs (5–10 nm) grown on template NTs (e.g., carbon and/or BN NTs). Right: ultrafine SW-MoS₂ NTs (<2 nm) confined within 1D spaces (this work). (B) Structural models of a SW-MoS₂ NT encapsulated inside a BN NT (top), illustrating the coaxial semiconductor/insulator heteroNT geometry (bottom). (C) Calculated bandgaps of armchair MoS₂ NTs as a function of diameter. The curve represents a guide to the eye. The gray dashed line marks the bandgap of monolayer MoS₂.

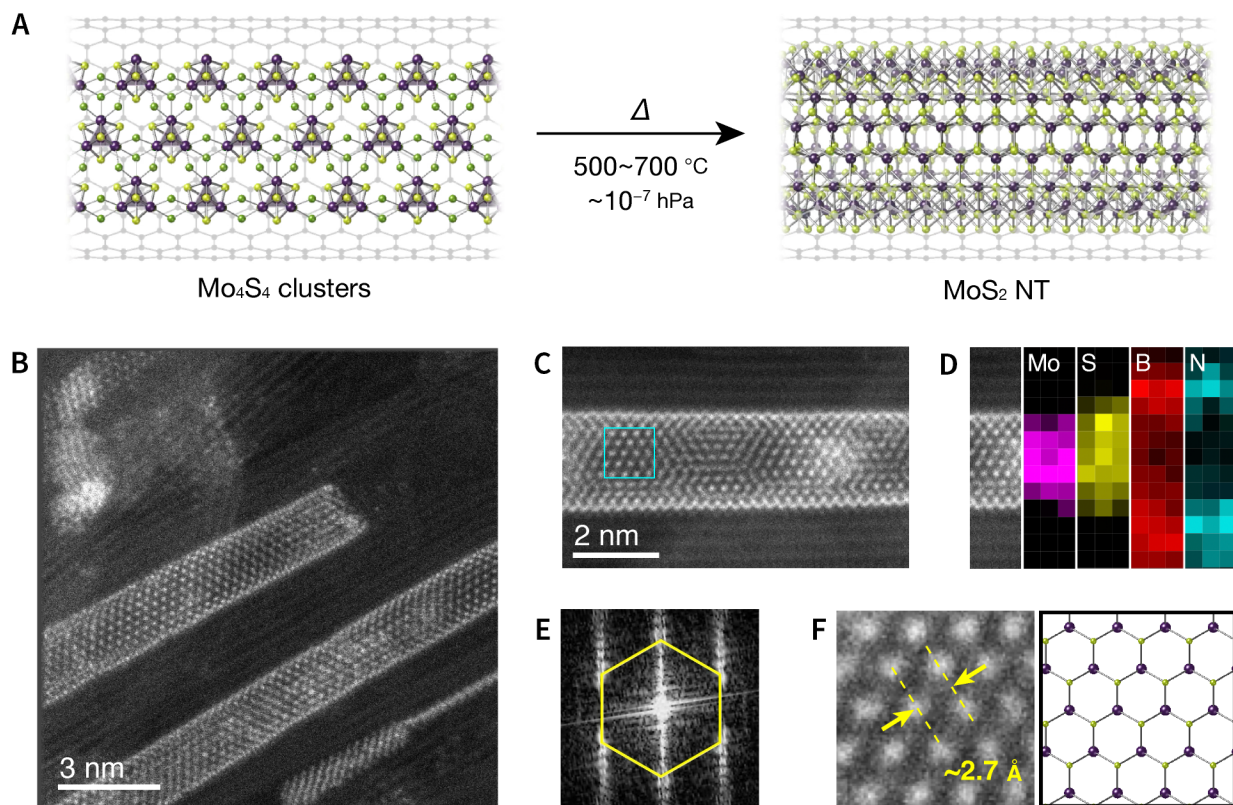


Fig. 2. Confined growth of SW-MoS₂ NTs inside BN NTs. (A) Schematic illustration of the transformation from Mo₄S₄ clusters to MoS₂ NTs under annealing. (B) HAADF image of SW-MoS₂ NTs coaxially grown within host BN NTs. (C) Magnified HAADF image of an individual SW-MoS₂@BN NT and (D) the corresponding EELS elemental maps demonstrating Mo and S localization in the inner NT. (E) FFT pattern acquired from the region in (C), displaying hexagonal symmetry consistent with MoS₂. (F) Magnified HAADF image of the boxed area in (C) and the corresponding structural model.

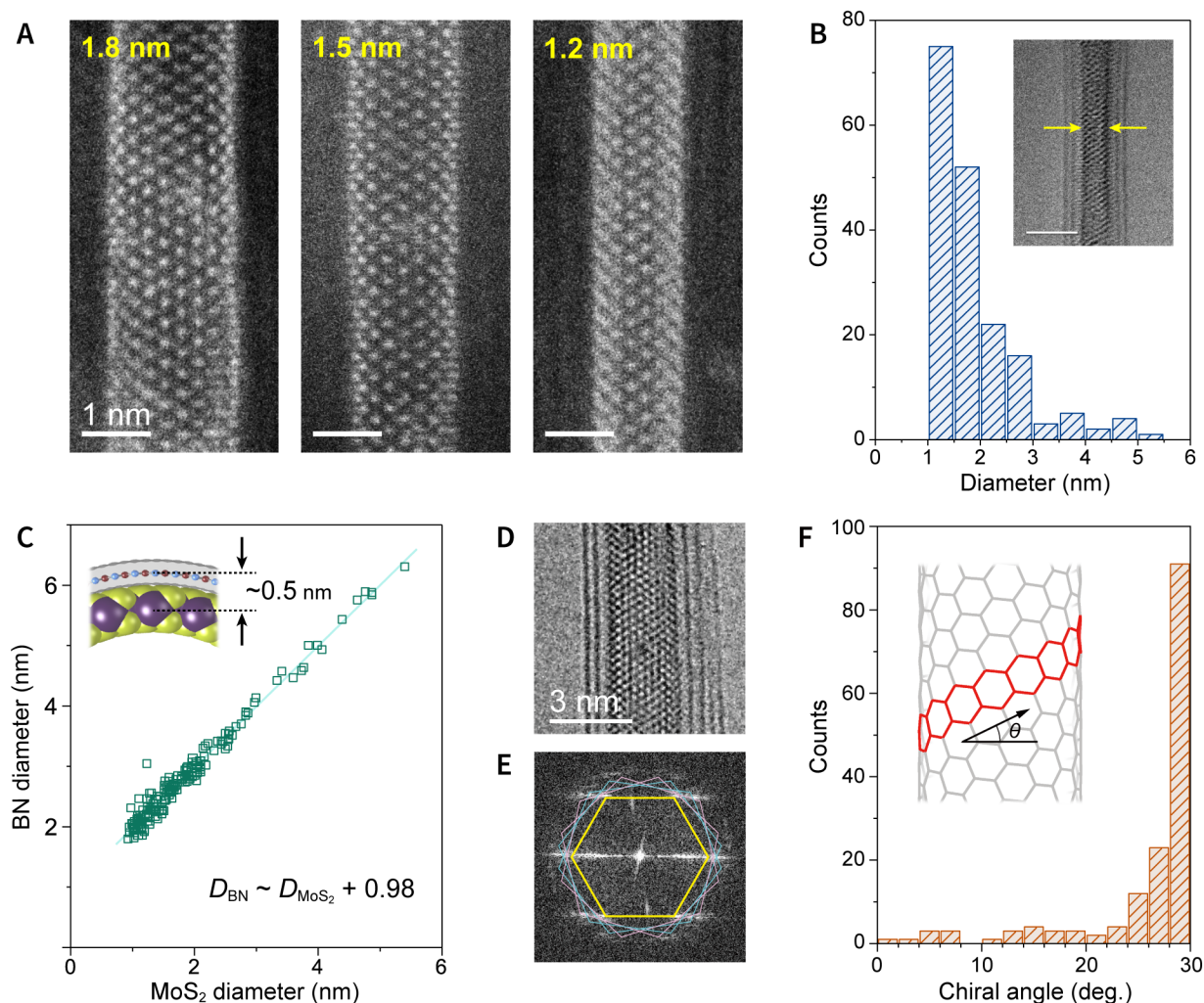


Fig. 3. Structural statistics of confined SW-MoS₂ NTs. (A) Atomic-resolution HAADF images of sub-2-nm SW-MoS₂ NTs. (B) Diameter distribution of 142 SW-MoS₂ NTs confined inside BN NTs. Inset: representative TEM image of a MoS₂ NT with a diameter of ~1 nm (Scale bar, 2 nm). (C) Correlation between the diameters of MoS₂ NTs and innermost BN NT shells. Inset: schematic cross-sectional model of a MoS₂@BN NT. (D) Representative TEM image of an individual MoS₂@BN NT and (E) the corresponding FFT pattern, highlighting contributions from the BN NT (cyan and pink) and the MoS₂ NT (yellow). (F) Chiral-angle distribution of 172 encapsulated SW-MoS₂ NTs (bin width, 2°). The rightmost bin contains the armchair configuration (28–30°). Inset: definition of the chiral angle θ for MoS₂ NTs.

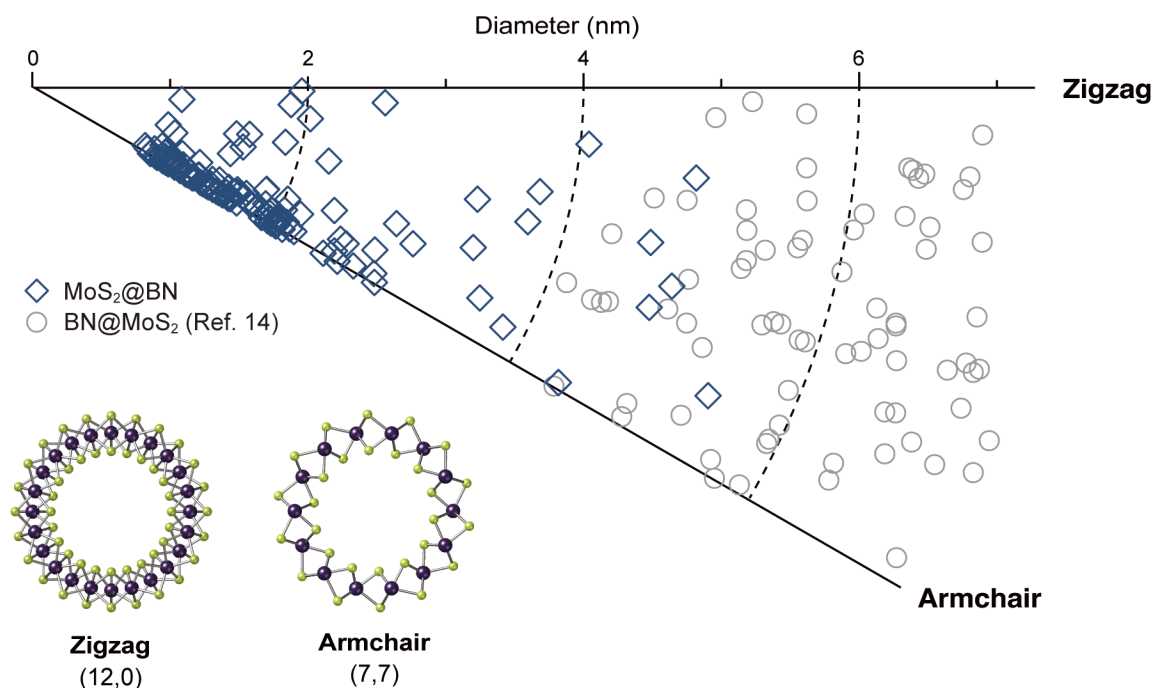


Fig. 4. Chirality distribution of confined SW-MoS₂ NTs. Chiral map of SW-MoS₂ NTs confined inside BN NT cavities (blue diamond) and on outer BN NT surfaces (gray circles). The inset shows cross-sectional structures of structurally optimized zigzag (12, 0) and armchair (7, 7) MoS₂ NTs with comparable diameters (~1.2 nm).

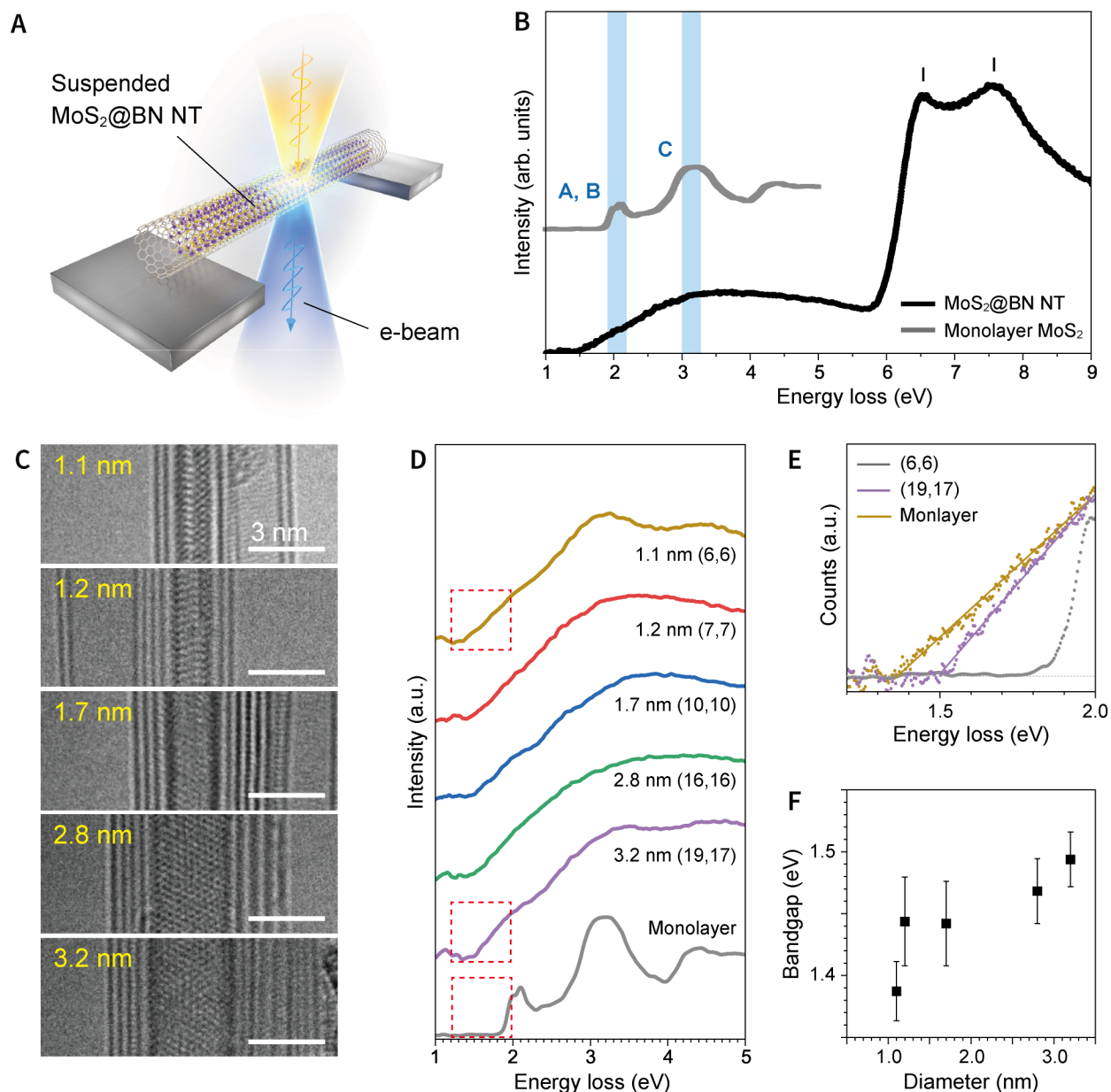


Fig. 5. Diameter-dependent optical properties of confined SW-MoS₂ NTs. (A) Schematic of the STEM-EELS setup used to probe suspended $\text{MoS}_2@\text{BN}$ NTs. (B) Low-loss EEL spectrum of a 1.6-nm-diameter SW-MoS₂ NT compared with monolayer MoS₂. The peaks at 6.5 eV and 7.6 eV correspond to the exciton and π plasmon of the BN NT, respectively. (C) Aberration-corrected TEM images of SW-MoS₂ NTs with diameters ranging from 1.1 to 3.2 nm (Scale bars, 3 nm). (D) Background-subtracted low-loss EEL spectra for the MoS₂ NTs shown in (C). (E) Enlarged view of the spectral onset for (6, 6) and (19, 17) species, compared with monolayer MoS₂. (F) Diameter dependence of the optical bandgap, extracted from the x-intercepts of linear fits to the onset region in the low-loss EEL spectra.



Supplementary Materials for

Confined growth of armchair MoS₂ nanotubes at the 1-nm limit

Yusuke Nakanishi,* Ryosuke Senga,* Shinpei Furusawa, Yuta Sato, Zheng Liu, Takumi Tanaka, Yanlin Gao, Mina Maruyama, Susumu Okada, Yasumitsu Miyata, and Kazu Suenaga*

Corresponding author: naka24ysk@edu.k.u-tokyo.ac.jp (Y.N.); ryosuke-senga@aist.go.jp (R.S.); suenaga-kazu@sanken.osaka-u.ac.jp (K.S.)

The PDF file includes:

Materials and Methods
Supplementary Text
Figs. S1 to S16
Tables S1 to S3

Materials and Methods

Sample preparation and characterization

Commercially available MoCl_5 (99.9%) and sulfur (99.9%) (purchased from Sigma Aldrich) were used as precursors. BN NTs (purchased from BNNT, LLC) were subjected to oxidative annealing in air (typically 800 °C for 90 min) to open the tube ends, followed by high-temperature annealing (1000 °C for 20 h) under $\sim 10^{-6}$ hPa to remove residual impurities and to clean inner cavities. The open-ended BN NTs (~ 5 mg) were mixed with MoCl_5 (27.4 mg) and sulfur (6.4 mg) and sealed in a Pyrex ampule under vacuum ($\sim 10^{-7}$ hPa). The sealed ampoule was kept at 500 °C for 2 h and then cooled to room temperature. The encapsulating BN NTs were sealed in a straight quartz ampule under vacuum ($\sim 10^{-7}$ hPa) and annealed at 500–700 °C for 20 h. Raman spectra of the samples were taken in a backscattering configuration using a micro-Raman setup (inVia, Renishaw) at 532 nm excitation. A 100 \times microscope objective (numerical aperture, NA = 0.9) was used to focus the laser beam and collect scattered light.

TEM/STEM imaging

HAADF-STEM images were taken using a cold field emission gun (JEM-ARM200F, ACCELARM) operated at 120 kV and equipped with a CEOS ASCOR corrector. Typically, 10 HAADF images were summed after drift compensation, with each image having a dwell time of 3–5 $\mu\text{s}/\text{pixel}$. STEM-EELS elemental maps of MoS_2 NTs were obtained based on $L_{2,3}$ edge signal intensities of sulfur, $M_{2,3}$ edge signal intensities of molybdenum, respectively. TEM observation was performed using a JEOL JEM-2100F-based electron microscope equipped with double JEOL Delta spherical aberration correctors operated at an electron accelerating voltage of 60 kV.

Low-loss EELS

Low-loss EELS measurements were performed using a TEM (JEOL Triple C#2) equipped with DELTA-type spherical aberration correctors and a double Wien filter-type monochromator. The measurements were performed at room temperature, with an energy resolution of approximately 50 meV (full width at half maximum). In this condition, the probe current was about 20 pA. All the spectra shown in Fig. 5 were collected at STEM mode operated at 60 kV. The convergence semiangle was 50 mrad while the inner semi-angle of the ADF detector and that for EELS collection were set to approximately 55 and 60 mrad, respectively. The EEL spectra were acquired using a Gatan GIF spectrometer (Quantum) optimized for low acceleration voltages. The EELS spectra were energetically calibrated using simultaneously obtained unsaturated zero-loss peaks. The background in the spectra shown in Fig. 5D was subtracted using a power-law function, with a fitting window approximately 1.0 eV wide, positioned around 1.0–1.2 eV where slight adjustments made for each spectrum.

DFT calculations

The geometric and electronic structures of isolated MoS_2 NTs are calculated based on the density functional theory with the generalized gradient approximation and ultrasoft pseudopotentials implemented in the STATE program package. For the structural optimization of armchair and zigzag NTs, we used 5- k point sampling along the tube axis, respectively. For the density states calculations, we carried out the calculations with 30- k and 20- k points for armchair and zigzag NTs, respectively. The valence wavefunction and deficit charge are expanded using the plane-wave basis set with cutoff energies of 25 and 225 Ry, respectively.

Statistical analysis

All the data were collected from the HAADF images. The standard deviation of the data was presented in the form of “mean \pm SD”. The statistical analyses were performed with OriginPro 2025.

Supplementary Text

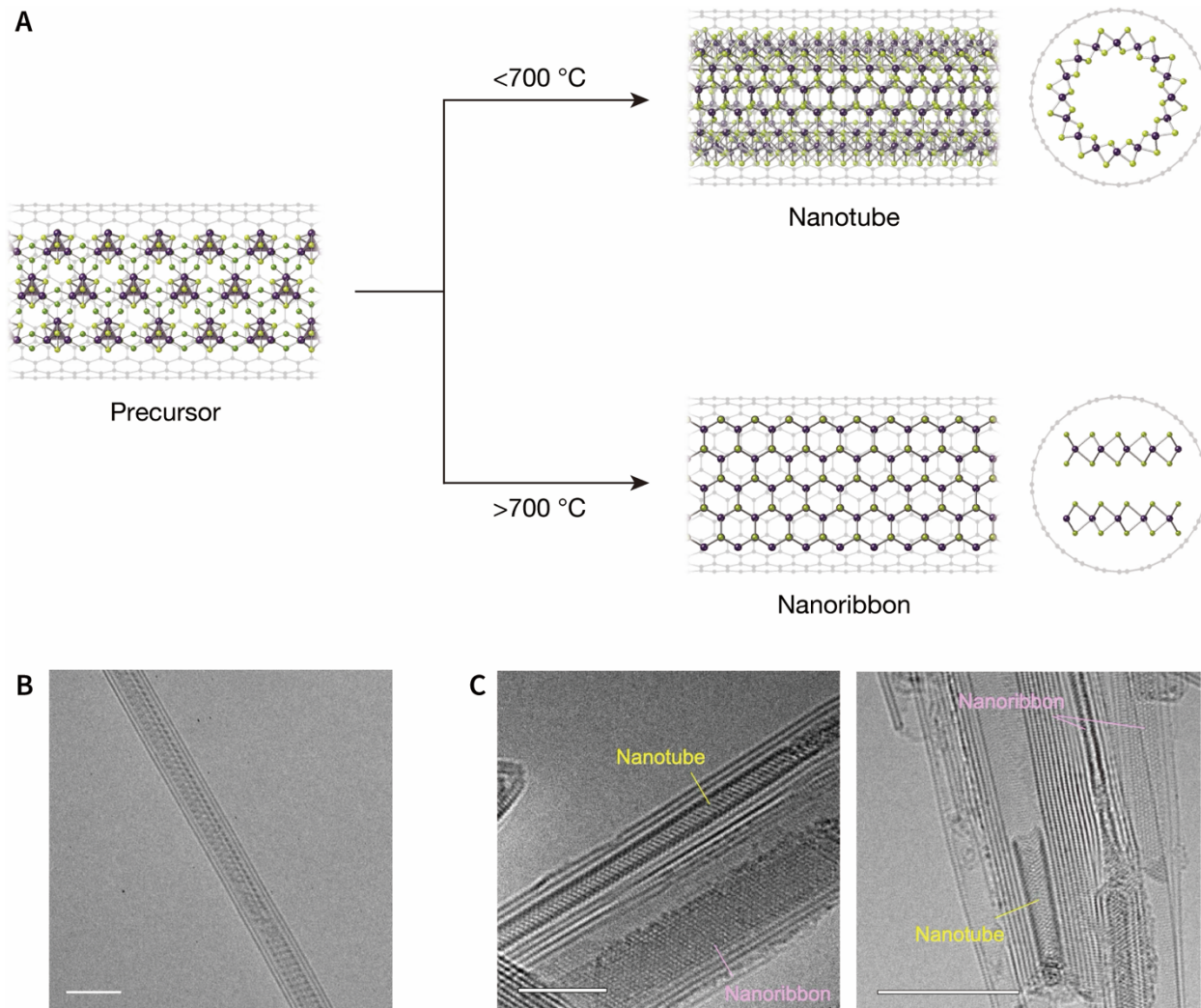


Fig. S1.

Thermal annealing of Mo_4S_4 clusters encapsulated within a BN NT. (A) Mo_4S_4 clusters encapsulated within a BN NT transform into 1D structures upon thermal annealing. Depending on the reaction temperature, the confined clusters convert either into a NT (<700 °C) or a nanoribbon (>700 °C). (B) TEM image of Mo_4S_4 clusters confined within a BN NT. The clusters are interconnected through Cl-mediated cross-linking (16). (C) TEM images of 1D products obtained after annealing at 700 °C, showing the coexistence of NTs and nanoribbons. Thermal annealing at 700 °C results in the simultaneous formation of NTs and nanoribbons. At higher temperatures, bilayer nanoribbons become the dominant product (17). At the few-nanometer dimensions, bilayer nanoribbons are thermodynamically more stable than highly curved NTs. Recent studies have shown that bilayer nanoribbons can transform into NTs within larger-diameter carbon NTs, where the curvature-induced strain is substantially lower than in the present BN NT templates (28). These observations suggest that the structural preference is strongly dependent on the diameter of BN NTs.

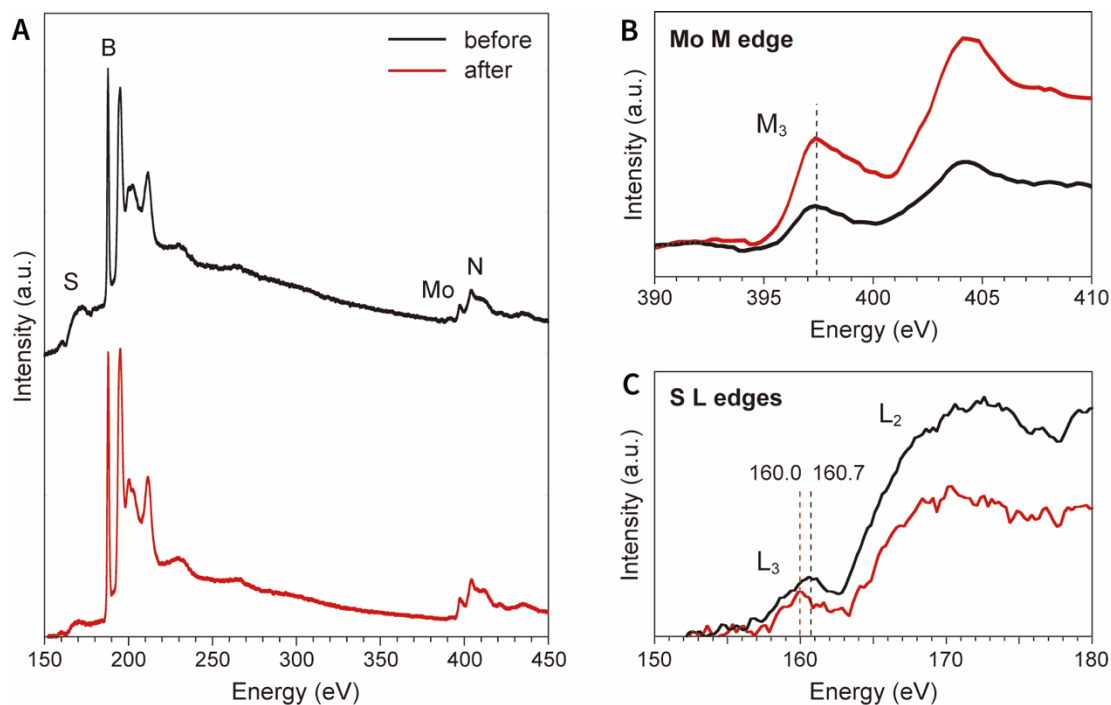


Fig. S2.

Core-loss EELS analysis of the encapsulating BN NTs before and after annealing. (A) Typical core-loss EEL spectra acquired from the filled BN NTs before and after annealing, showing Mo and S signals from the guest species, along with B and N from the BN NT host. (B, C) Magnified views of the Mo M₃ edge and S L_{2,3} edge regions. The Mo M₃ edge remains essentially unchanged after annealing, whereas the S L₃ edge exhibits a slight shift towards lower energy. This shift likely reflects differences in the sulfur bonding environments of between Mo₄S₄ and MoS₂, as sulfur atoms in Mo₄S₄ are in a higher oxidation state than in MoS₂.

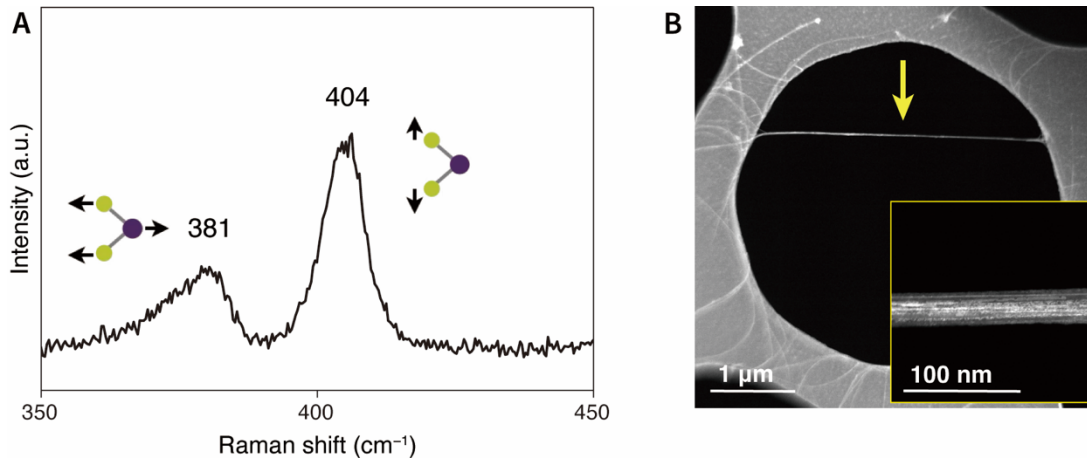


Fig. S3.

Raman characterization of the encapsulated MoS₂@BN NTs. (A) Raman spectrum of the encapsulated MoS₂ NTs. (B) HAADF image of the suspended MoS₂@BN NT bundle used for the Raman measurement. The spectrum was collected from an individual bundle suspended across a pore in a TEM grid. Given the minimal residues on the outer BN NT walls, the observed signals are attributed to the encapsulated MoS₂ NTs. The Raman spectrum exhibits two characteristic modes at 381 cm⁻¹ (in-plane E' mode) and 404 cm⁻¹ (out-of-plane A' mode). Compared with monolayer MoS₂ (E' = 384–386 cm⁻¹ and A' = 403–405 cm⁻¹), the low-frequency shift of the E' mode indicates tensile strain associated with curvature-induced lattice distortion (29). The E' mode also exhibits broadening relative to monolayer MoS₂, consistent with strain inhomogeneity arising from diameter variation.

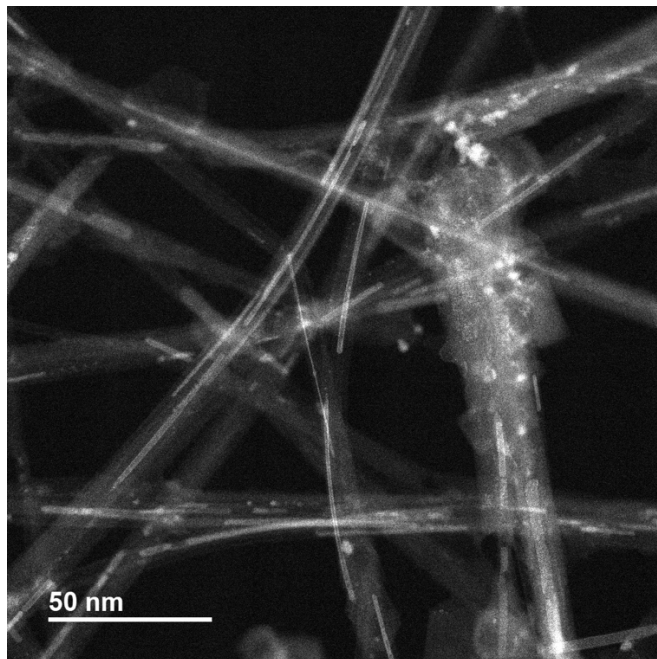


Fig. S4.

Additional HAADF image of the as-grown samples. An overview HAADF image of filled BN NTs is shown. The bright linear features correspond to the encapsulating MoS₂ NTs. Some MoS₂ NTs with lengths exceeding 150 nm are observed.

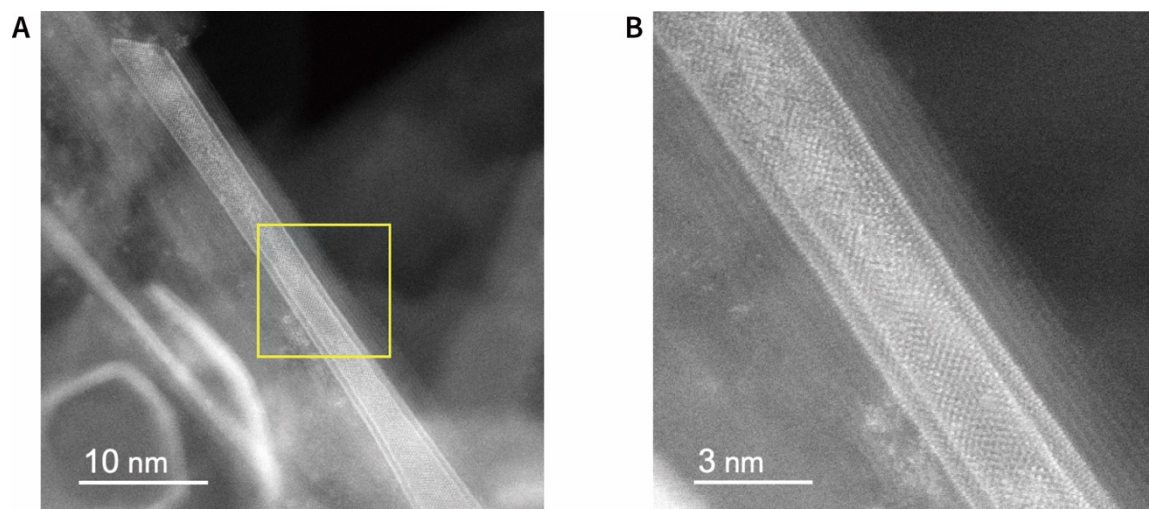


Fig. S5.
HAADF images of DW-MoS₂ NTs confined within BN NTs. (A) HAADF image of a DW-MoS₂ NT formed inside a multiwalled BN NT. (B) Magnified view of the region highlighted in (A), revealing the two concentric MoS₂ walls.

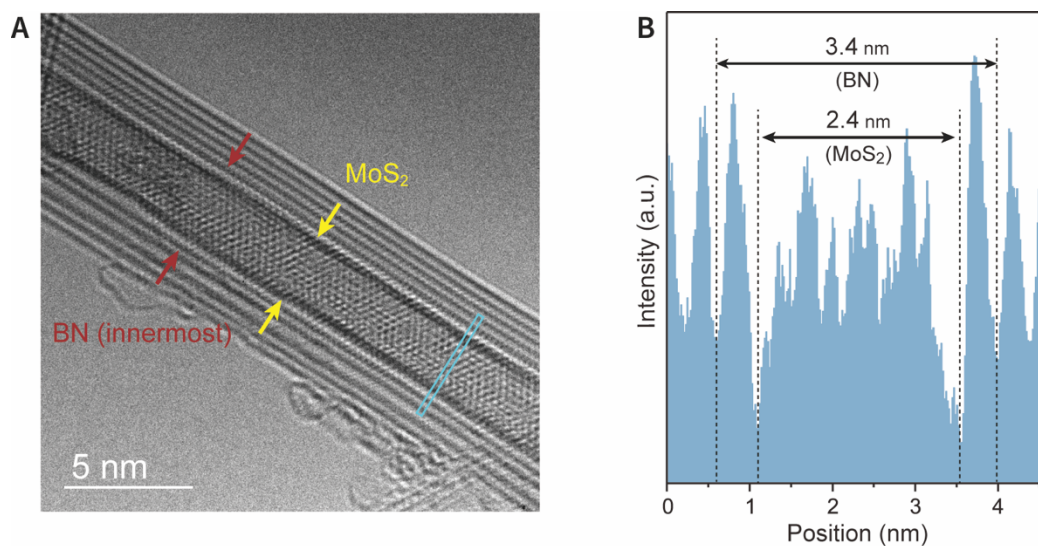


Fig. S6.

Diameter correlation between the BN host and MoS₂ guest. (A) A representative HAADF image of an individual MoS₂@BN NT, showing that the innermost BN wall fit well with the confined MoS₂ NT. (B) Intensity line profile extracted from the region highlighted in (A), used to determine the respective diameters of the BN NT host and MoS₂ NT guest.

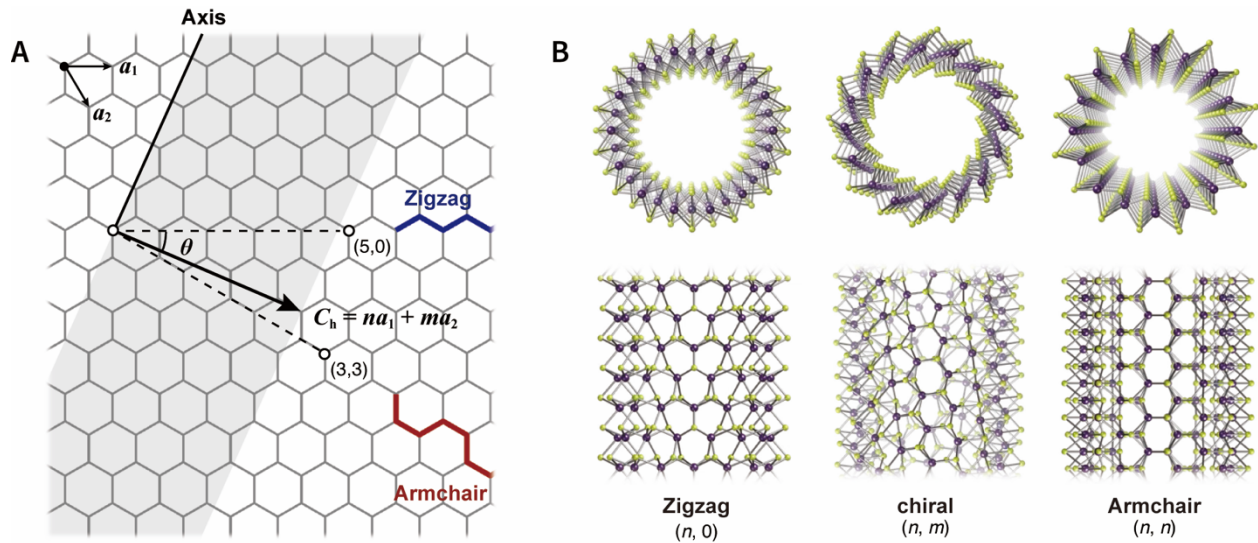


Fig. S7.

Chirality and atomic structures of MoS₂ NTs. (A) Definition of the chiral indices (n, m) for SW-MoS₂ NTs. The chiral vector (black solid line) is mapped onto a hexagonal MoS₂ defined by basis vectors a_1 and a_2 . Achiral configurations correspond to zigzag $(n, 0)$ and armchair (n, n) limits, with chiral angle $\theta = 0$ and 30° , respectively. (B) Structural models of zigzag, chiral, and armchair MoS₂ NTs.

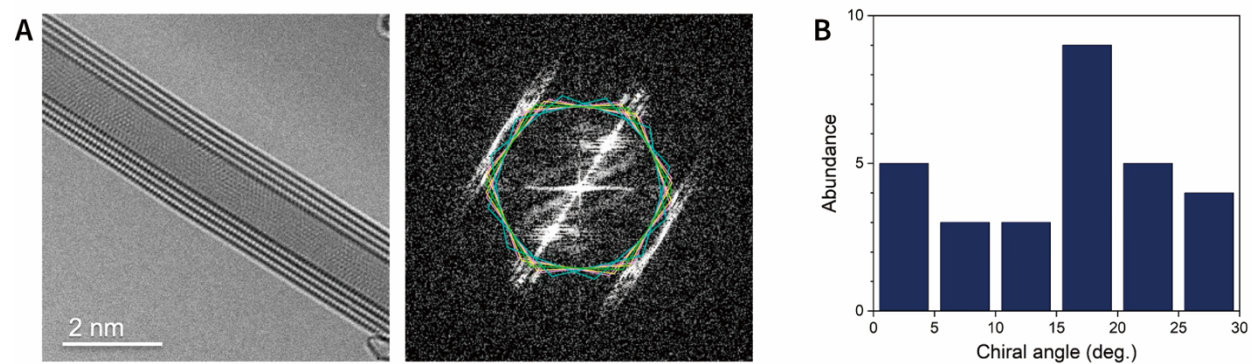


Fig. S8.

Chiral-angle distribution of the employed BN NTs. (A) Representative TEM image of a multiwalled BN NT (4 walls) and the corresponding FFT pattern, from which the chiral angle was determined. (B) Chiral-angle distribution of 29 DW-BN NTs used in the present experiments. The inner and outer walls were not distinguished in the present analysis.

Table S1.
Geometrical parameters of armchair MoS₂ NTs. Chiral angles and diameters of 91 SW-MoS₂ NTs with $\theta = 28\text{--}30^\circ$.

Sample	Chiral angle (deg.)	Diameter (nm)	Sample	Chiral angle (deg.)	Diameter (nm)	Sample	Chiral angle (deg.)	Diameter (nm)
1	30.0	2.87	31	30.0	1.34	61	29.5	4.39
2	30.0	2.79	32	30.0	1.31	62	29.4	2.04
3	30.0	2.56	33	30.0	1.29	63	29.4	2.67
4	30.0	2.44	34	30.0	1.28	64	29.3	3.99
5	30.0	2.09	35	30.0	1.28	65	29.2	1.97
6	30.0	2.09	36	30.0	1.24	66	29.2	2.18
7	30.0	2.04	37	30.0	1.23	67	29.2	2.14
8	30.0	2.04	38	30.0	1.22	68	29.1	1.63
9	30.0	2.00	39	30.0	1.19	69	29.1	1.63
10	30.0	1.97	40	30.0	1.19	70	29.0	1.61
11	30.0	1.92	41	30.0	1.14	71	28.9	2.83
12	30.0	1.90	42	30.0	1.13	72	28.9	1.30
13	30.0	1.74	43	30.0	1.12	73	28.8	1.47
14	30.0	1.71	44	30.0	1.10	74	28.8	2.50
15	30.0	1.69	45	30.0	1.09	75	28.8	2.03
16	30.0	1.64	46	30.0	1.09	76	28.8	1.81
17	30.0	1.63	47	30.0	1.09	77	28.7	1.90
18	30.0	1.60	48	30.0	1.09	78	28.7	0.95
19	30.0	1.59	49	30.0	1.05	79	28.7	2.09
20	30.0	1.56	50	30.0	1.04	80	28.6	2.03
21	30.0	1.54	51	30.0	1.03	81	28.5	1.18
22	30.0	1.53	52	30.0	1.03	82	28.5	1.81
23	30.0	1.51	53	30.0	1.03	83	28.5	1.37
24	30.0	1.47	54	30.0	1.01	84	28.4	1.63
25	30.0	1.45	55	30.0	0.99	85	28.3	1.85
26	30.0	1.43	56	30.0	0.98	86	28.3	2.09
27	30.0	1.41	57	29.8	1.66	87	28.3	1.96
28	30.0	1.41	58	29.8	1.13	88	28.3	1.14
29	30.0	1.39	59	29.7	1.47	89	28.3	3.16
30	30.0	1.35	60	29.7	1.14	90	28.3	1.38
						91	28.2	1.09

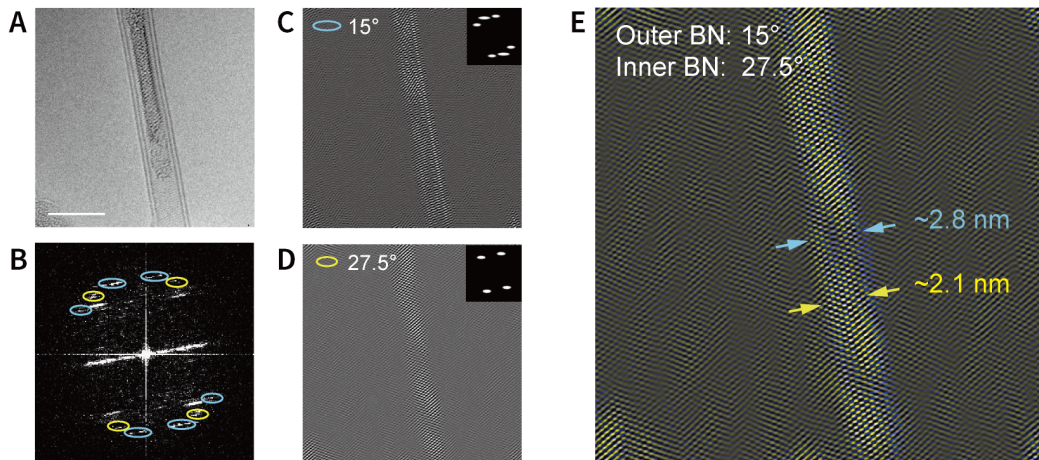


Figure S9.

Chiral-angle analysis of inner and outer walls in DW-BN NTs. (A) TEM image and (B) the corresponding FFT pattern of a representative SW-MoS₂@DW-BN NT. (C, D) Inverse FFT images obtained by applying masks on the FFT pattern in (B), isolating the contributions from the inner and outer BN walls. (E) Overlay of the inverse FFT images in (C) and (D), illustrating the distinct chiral angles and diameters of the inner and outer BN walls.

Table S2.

Summary of host–guest chiral-angle analysis in MoS₂@BN NTs. Chiral angles of the encapsulated MoS₂ NTs and the corresponding inner and outer BN walls in the host SW- and DW-BN NTs. Sample 1–3 correspond to SW-BN NTs, whereas Samples 4–9 are DW-BN NTs.

Sample	MoS ₂ (deg.)	Inner BN (deg.)	Outer BN (deg.)
1	30.0	2.8	—
2	28.5	24.4	—
3	24.6	27.4	—
4	30.0	11.7	18.9
5	29.9	3.1	19.1
6	29.4	16.4	23.0
7	29.1	30.0	8.9
8	27.4	17.4	23.4
9	26.1	27.5	15.0

For DW-BN NTs, the chiral angles of the inner and outer walls were determined by combining FFT analysis with inverse FFT reconstruction to isolate the respective wall contributions. The absolute orientation of each wall was further confirmed by examining the atomic lattice arrangement along the sidewalls in the TEM images, assigning the wall closer to the zigzag configuration to the smaller chiral angle (30). For Sample 8, the assignments should be regarded as the most probable indices within experimental uncertainty.

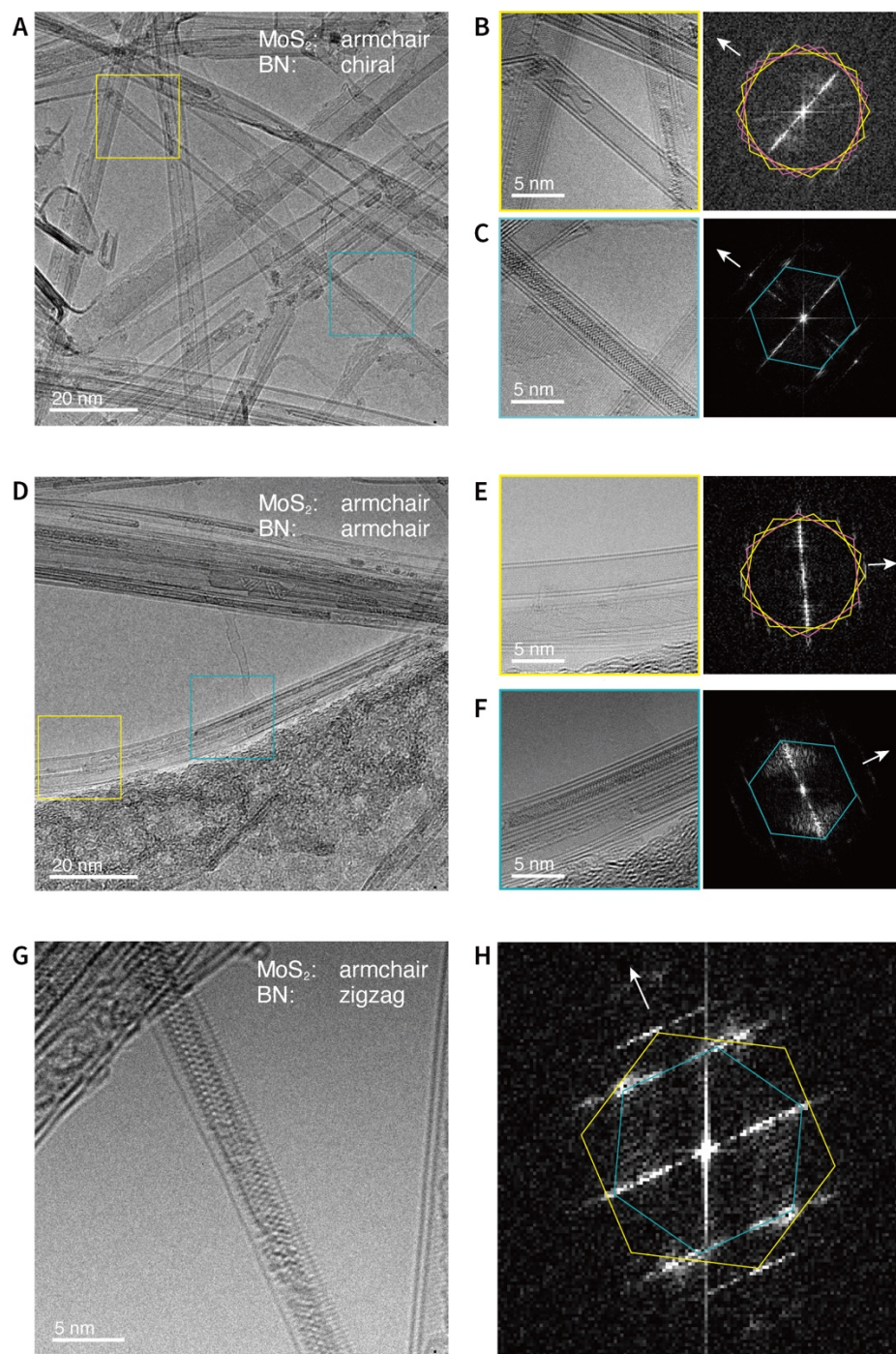


Fig. S10.

Representative host-guest chiral-angle relationships in MoS₂@BN NTs. (A) TEM image of a SW-MoS₂@DW-BN NT (Sample 4 in table S2). (B, C) Magnified TEM images and corresponding FFT patterns acquired from the yellow and cyan boxed regions in (A), respectively. (D) TEM image of Sample 7. (E, F) Magnified TEM images and corresponding FFT patterns from the yellow and cyan boxed regions in (D), respectively. (G) TEM image of Sample 1. (H) Corresponding FFT pattern of (G). White arrows indicate the NT axis.

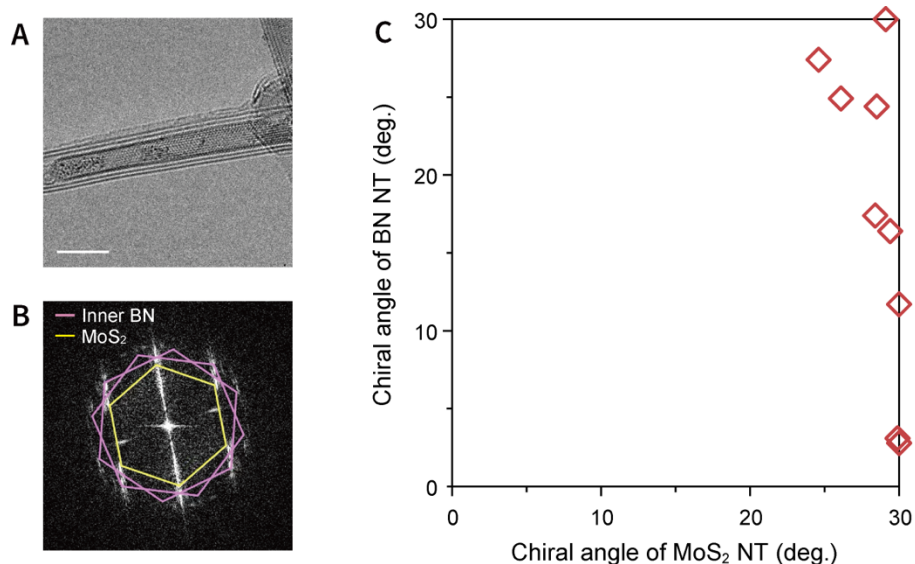


Fig. S11.

Chiral-angle relationship between encapsulated MoS₂ NTs and the inner BN NTs. (A) Representative TEM image of a SW-MoS₂@DW-BN NT (Sample 6 in table S2) (Scale bar, 5 nm). (B) FFT pattern of Sample 6, with reflections from the inner BN wall (pink) and the MoS₂ NT (yellow) highlighted. (C) Correlation between the chiral angles of MoS₂ NTs and the inner BN walls. Each data point corresponds to an individual MoS₂@BN NT listed in table S2 ($n = 9$). For DW-BN NTs, the chiral angle of the inner BN walls is plotted.

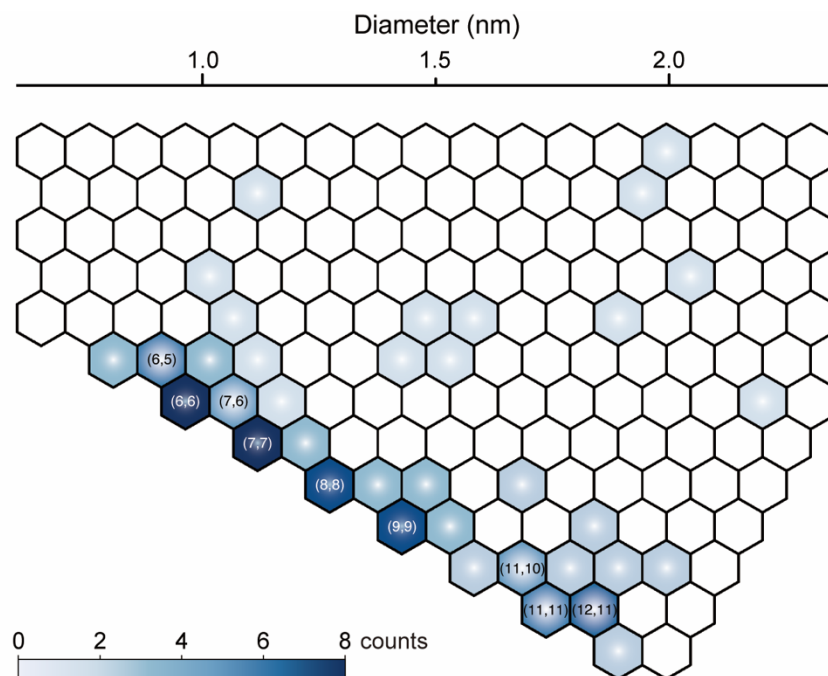


Fig. S12.

Chirality map of the encapsulated SW-MoS₂ NTs. Hexagonal map showing the (n, m) indices assigned to individual SW-MoS₂ NTs at few-nanometer diameters. Color shading demotes the occurrence frequency of each chirality.

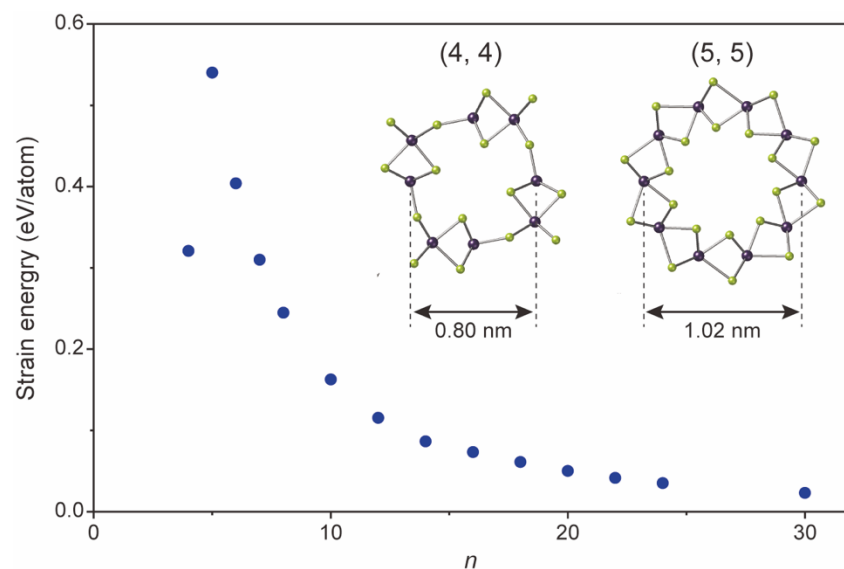


Fig. S13.

Calculated structural stability of armchair MoS_2 NTs. Strain energies (relative total energies) of (n, n) MoS_2 NTs as a function of the index n . The strain energies are measured from that of monolayer MoS_2 .

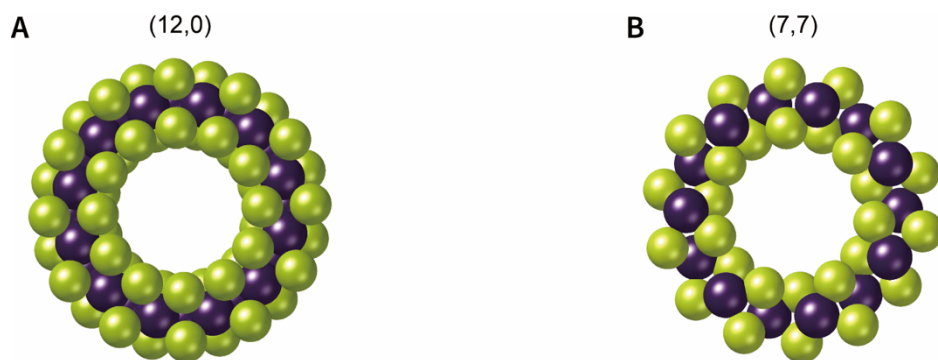


Fig. S14.
Comparison of zigzag and armchair MoS₂ NTs. Space-filling models of theoretically optimized (A) zigzag (12, 0) and (B) armchair (7, 7) MoS₂ NTs, both with diameters of ~1.2 nm.

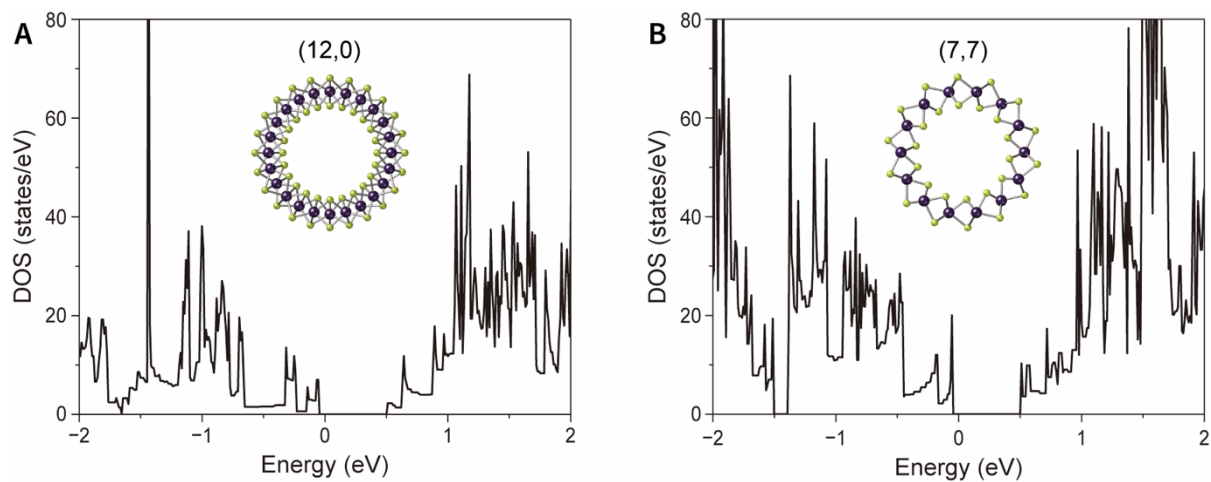


Fig. S15.

Density of states of zigzag and armchair species. DFT-calculated electronic density of states (DOS) for (A) zigzag (12, 0) and (B) armchair (7, 7) MoS₂ NTs.

Table S3.
Chiral indices, diameters, and fitting parameters of MoS₂ NTs analyzed by low-loss EELS.
The absorption onset was determined by linear fitting over the energy range of 1.5–2.0 eV. Values in parentheses denote the standard errors of the fits.

MoS ₂ NT		Fitting parameters		
Chiral indices	Diameter (nm)	Slope	y-intercept	x-intercept
(6, 6)	1.1	0.195 (0.002)	-0.270 (0.004)	1.387 (0.024)
(7, 7)	1.2	0.140 (0.002)	-0.202 (0.004)	1.444 (0.036)
(10, 10)	1.7	0.157 (0.002)	-0.226 (0.004)	1.442 (0.034)
(16, 16)	2.8	0.162 (0.002)	-0.238 (0.003)	1.468 (0.026)
(19, 17)	3.2	0.267 (0.003)	-0.39934 (0.0045)	1.494 (0.022)

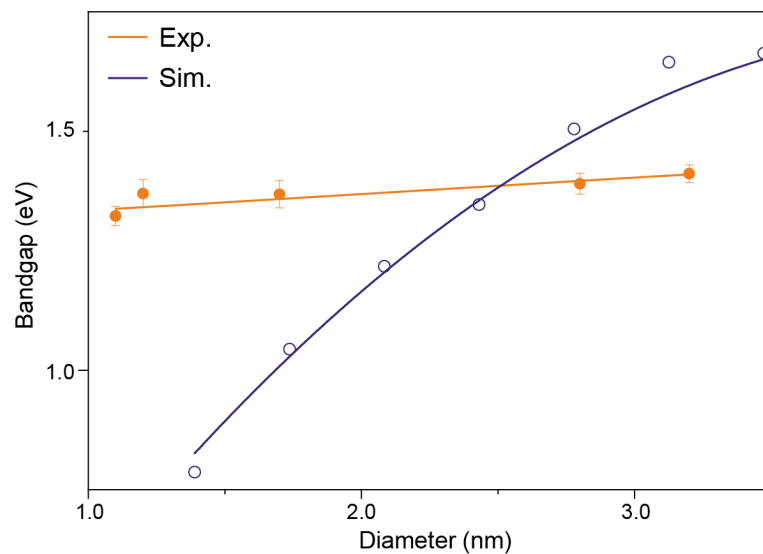


Fig. S16.

Diameter dependence of the experimental optical bandgaps and DFT-calculated bandgaps of few-nanometer MoS₂ NTs. Experimental bandgaps were determined from the x -intercepts of linear fits to the absorption onset in the low-loss EEL spectra (Fig. 5C). The calculated values correspond to ground-state DFT bandgaps (Fig. 1C).